Draft version March 15, 2024
Typeset using LaTeX **twocolumn** style in AASTeX631

Near-Infrared Ca II Triplet As A Stellar Activity Indicator: Library and Comparative Study

X.Huang (黄鑫)[1,2,*] Yuji He (何玉吉)[1,2] Bai Zhong-Rui (白仲瑞)[1,2] Hai-Long Yuan (袁海龙)[1,2]
Mingkuan Yang (杨明宽)[1,2] Ming Zhou (周明)[1] Yiqiao dong (董义乔)[1] Mengxin Wang (汪梦欣)[1,2]
Han He (贺晗)[3,2,†] Jinghua Zhang (张敬华)[4] Yaoquan Chu (褚耀泉)[5] Yongheng Zhao (赵永恒)[1,2]
Yong Zhang (张勇)[1,2] and H.T.Zhang (张昊彤)[1,2,‡]

[1]CAS Key Laboratory of Optical Astronomy, National Astronomical Observatories, Chinese Academy of Sciences, Beijing 100101, China
[2]School of Astronomy and Space Science, University of Chinese Academy of Sciences, Beijing 100049, China
[3]National Astronomical Observatories, Chinese Academy of Sciences, Beijing 100101, China
[4]South-Western Institute for Astronomy Research, Yunnan University, Chenggong District, Kunming 650500, China
[5]University of Science and Technology of China, Hefei 230026, China

ABSTRACT

We have established and released a new stellar index library of the Ca II Triplet, which serves as an indicator for characterizing the chromospheric activity of stars. The library is based on data from the Large Sky Area Multi-Object Fiber Spectroscopic Telescope (LAMOST) Low-Resolution Spectroscopic Survey (LRS) Data Release 9 (DR9). To better reflect the chromospheric activity of stars, we have defined new indices R and R^+. The library includes measurements of R and R^+ for each Ca II infrared triplet (IRT) from 699,348 spectra of 562,863 F, G and K-type solar-like stars with Signal-to-Noise Ratio (SNR) higher than 100, as well as the stellar atmospheric parameters and basic information inherited from the LAMOST LRS Catalog. We compared the differences between the 3 individual index of the Ca II Triplet and also conducted a comparative analysis of $R^+_{\lambda 8542}$ to the Ca II H&K S and R^+_{HK} index databases. We observe the fraction of low active stars decreases with T_{eff} and the fraction of high active first decrease with decreasing temperature and turn to increase with decreasing temperature at 5800K. We also find a significant fraction of stars that show high activity index in both Ca II H&K and IRT are binaries with low activity, some of them could be discriminated in Ca II H&K S index and $R^+_{\lambda 8542}$ space. This newly stellar library serves as a valuable resource for studying chromospheric activity in stars and can be used to improve our comprehension of stellar magnetic activity and other astrophysical phenomena.

Keywords: Stellar activity; Stellar chromosphere; Astronomy databases.

1. INTRODUCTION

Stars with outer convective envelopes tend to exhibit magnetic activity. Star spots and faculae in the photosphere, plages in the chromosphere, X-rays in the corona are all related to magnetic activity. Studies of stellar activity are essential for improving our understanding of stellar dynamo models and the related studies such as the stellar age and rotation or activity relation, stellar flare and stellar activity cycle. On the other hand, stellar activity is important for exoplanets studies, since magnetic activity especially flares will have an impact on planetary habitability (Shields et al. 2016; Howard et al. 2018; Lillo-Box et al. 2022). Also, jitters in both photometry and radial velocity measurement caused by stellar magnetic activity will hinder the detection of earth like exoplanet (Wright 2005). Finding stars with low activity is crucial to those low mass exoplanets detecting.

The emission core of lines originating from the chromosphere can serve as indicators to quantify activity. One well-known measurement of activity is the Ca II H&K S_{MWO} index, proposed by the Mount-Wilson Observatory (Wilson 1968). However, the photosphere also contributes to the Ca II H&K lines flux, and the contribution varies with effective temperatures, leading to potential misestimation of stellar activity. To overcome this issue, Linsky et al. (1979a) proposed the R'_{HK} index, which subtracts the empirical photospheric flux

* huangxin@bao.ac.cn
† hehan@bao.ac.cn
‡ htzhang@bao.ac.cn

from the flux. Building on the R'_{HK} index, Mittag et al. (2013, 2019) proposed the R^{+}_{HK} index, which subtracts the basal flux in addition to the photospheric flux. H_α line can also serve as an indicator of activity and is more suitable for late-type stars than Ca II H&K (Cincunegui et al. 2007). They defined the S^{+} index for H_α, which correlates well with the S_{MWO} index.

The Ca II IRT lines represent another set of indices of activity:

$$8498.0\mathring{A}\ 4\ ^2P_{\frac{3}{2}} - 3\ ^2D_{\frac{3}{2}},$$
$$8542.1\mathring{A}\ 4\ ^2P_{\frac{3}{2}} - 3\ ^2D_{\frac{5}{2}},$$
$$8662.1\mathring{A}\ 4\ ^2P_{\frac{1}{2}} - 3\ ^2D_{\frac{3}{2}},$$

absorptions due to the Ca II IRT lines are clearly visible in the atmosphere of cool stars (see Tennyson 2019, chap. 6). The core of the Ca II IRT emission lines are formed in the lower chromosphere through subordinate transitions between the excited levels of Ca II $4\,^2P_{\frac{3}{2},\frac{1}{2}}$ and meta-stable $3\,^2D_{\frac{3}{2},\frac{5}{2}}$. These lines are mostly collision-controlled (de Grijs & Kamath 2021), and are highly sensitive to the ambient temperature (Cauzzi et al. 2008). They serve as indicators of stellar chromospheric activity, as demonstrated by Linsky et al. (1979b). Linsky et al. (1979b) proposed Ca II $\lambda 8542$ as an activity indicator, while Andretta et al. (2005) defined the R_{IRT} index based on the central depression in the Ca II IRT lines, taking into account rotational broadening. Notsu et al. (2015) employed $r_0(IRT)$, which is the residual flux normalized by the continuum at the line cores of IRT lines, and H_α to study superflares, suggested that the brightness variation of superflare stars can be explained by the rotation with large starspots. Žerjal et al. (2013) employed the observed spectra of non-active stars as a template and measured the template-subtracted equivalent width (EW) of the Ca II IRT lines to represent stellar activity.

It is important to build large databases to statistically understanding the physical mechanisms of stellar magnetic activity. As part of this effort, we have previously established large sample databases for solar-like stars' activity utilizing Ca II H&K (Zhang et al. 2022) and H$_\alpha$ (He et al. 2023) indices based on LAMOST spectra. In this study, we will build a stellar activity database of F, G, K stars based on the measurements of Ca II IRT lines.

LAMOST, the Large Sky Area Multi-Object Fiber Spectroscopic Telescope located in Xinglong, China, offers low-resolution spectra with a resolving power of $\lambda/\Delta\lambda = 1800$ covering the wavelength range of 3700-9100 $\mathring{A}$ (Zhao et al. 2012). Additionally, it provides Mid-Resolution Spectra (MRS) with $R \sim 7500$ in 4950-5350 $\mathring{A}$, 6300-6800$\mathring{A}$ band. The observed data is first reduced by LAMOST 2D pipeline (Bai et al. 2017, 2021), and then LAMOST stellar parameters pipeline (Wu et al. 2011) is applied. The released data including extracted spectra files as well as the stellar parameters are available at the LAMOST website, http://www.lamost.org.

There have been several studies of stellar activity based on LAMOST data. For example, Zhang et al. (2020) employed the R^{+}_{HK} index using LAMOST spectra to investigate the relationship between stellar activity, period, and the amplitude of brightness variation, along with Kepler light curve data; He et al. (2023) measured the R_{H_α} index using LAMOST MRS; Zhang et al. (2022) established Ca II H&K S index database based on LAMOST LRS; Karoff et al. (2016) explored superflares using the S index along with Kepler light curve data, they found that superflare stars are characterized by enhanced activity; Zhang et al. (2019) proposed that stellar chromospheric activity indices can be used to roughly estimate stellar ages for dwarfs. The above studies are based on the measurement of Ca II H&K or H_α, the capability of Ca II IRT lines has not been fully explored yet.

In this study, our focus is on the Ca II IRT lines of solar-like stars, all the spectra utilized come from the LAMOST LRS DR9 database. Due to the low spectral resolution, the core emission of lines is not sensitive to EW and may be compromised by deviations in rotation velocity estimations. Instead, we introduce a new R index that specifically considers the flux near the center of spectral lines. To remove the photospheric flux components, we employed the `BT-Settl` stellar spectral models (Allard et al. 1997, 2011, 2013) and calculated the template-subtracted index, R^{+}, to represent pure activity levels. Furthermore, we compared our results with the existing database of Ca II H&K lines and discussed the nature of stars in the distributions of Ca II H&K and IRT activity indices.

This paper is organized in six sections. Section 2 introduces the data selection criteria, while Section 3 defines the indices R and R^{+} and provides a detailed description of the data processing steps. Section 4 shows the detail of our database. In Section 5 we compared the strengths of the three lines, discusses the relationship and differences between the indices measured from Ca II H&K. Section 6 is the summary.

2. DATA PREPARATION

Our analysis is centered on F, G and K-type solar-like stars, and all stellar parameters sourced from the catalog: `LAMOST LRS Stellar Parameter of A, F, G, and K Stars` (*AFGK* Catalog) (http://www.lamost.

org/dr9/). To ensure comparability with the prior Ca II H&K index study by Zhang et al. (2022), the following parameter restrictions are applied:

1. $100 \leq SNR_i,\ SNR_z$. This is to ensure the high quality of the Ca II IRT lines located between the i & z band.

2. $4800K \leq T_{eff} \leq 6800K$, This criterion is same as Zhang et al. (2022), the temperature range of solar-like stars covers most F, G, K samples in the $AFGK$ Catalog.

3. For surface gravity, the empirical formulas of Zhang et al. (2022) is adopted to select main sequence stars:

$$5.98 - 0.00035T_{eff} \leq \log g \leq 5.0$$

After rejecting spectra with issues such as fiber failure in the IRT bandpass, heavy skylight pollution, and wavelength calibration failure, we selected a total of 699,348 spectra from the LAMOST database. Considering multiple observations for the same star, these spectra correspond to 562,863 stars. The number of spectra cross-correlated with the previous work of Ca II H&K S and R^+_{HK} index databases is listed in Table 1.

Table 1. Ca II index Database Using LAMOST Data

Database	Spectra Number	Common Spectra
Ca II IRT R, R^+	699348	-
Ca II H&K S	1330654	574780
Ca II H&K R^+_{HK}	59816	14028

NOTE—IRT R, R^+ database is presented in this work. S index and R^+_{HK} databases are provided by Zhang et al. (2022) and Zhang et al. (2020), respectively.

3. METHOD

3.1. *Index definitions*

We defined R, R^+ index for each line of Ca II IRT as following equations:

$$R = \frac{1}{\lambda_2 - \lambda_1} \int_{\lambda_1}^{\lambda_2} \frac{F_o(\lambda)}{C_o(\lambda)}\, d\lambda, \tag{1}$$

$$R^+ = \frac{1}{\lambda_2 - \lambda_1} \int_{\lambda_1}^{\lambda_2} \frac{F_o(\lambda)}{C_o(\lambda)} - \frac{F_m(\lambda)}{C_m(\lambda)}\, d\lambda, \tag{2}$$

where $F(\lambda)$ is the spectrum, $C(\lambda)$ is the linear function fitting the local continuum in the IRT bandpass, and subscripts ”o” and ”m” stand for observation and model, respectively. The normalized spectrum is expressed as $F(\lambda)/C(\lambda)$. λ_1, λ_2 are the starting and ending wavelengths of the sampling range, which is $1\AA$ around the central wavelength of each Ca II IRT lines. The corresponding central wavelengths and the sampling ranges are listed in Table 2. As the LAMOST spectral data points are in approximately $2\AA$ intervals, a cubic spline function is applied to interpolate the spectrum to **a finer grid**.

Table 2. Sampling Range for Ca II IRT Index

Lines	Center($\AA$)	Bandpass($\AA$)
Ca II λ8498	8500.35	8549.85-8500.85
Ca II λ8542	8544.44	8543.94-8544.94
Ca II λ8662	8664.52	8664.02-8665.02

NOTE—The wavelength are in vacuum, as provided by LAMOST data release(LAMOST LRS DR9).

LAMOST DR9 provides normalized spectra for most spectra, typically generated for the entire spectrum. To achieve a better performance, we re-normalized the spectra within the IRT bandpass with a normalization method that utilizes the `LinearLSQFitter` provide by `Astropy` module, which is a linear least square fitting method (Robitaille et al. 2013; Price-Whelan et al. 2018, 2022). Two examples are illustrated in Figure 1 to show the difference between global and local normalization. Both methods perform similarly for the absorption line spectra, but in the case of emission lines, our method clearly outperforms the LAMOST approach.

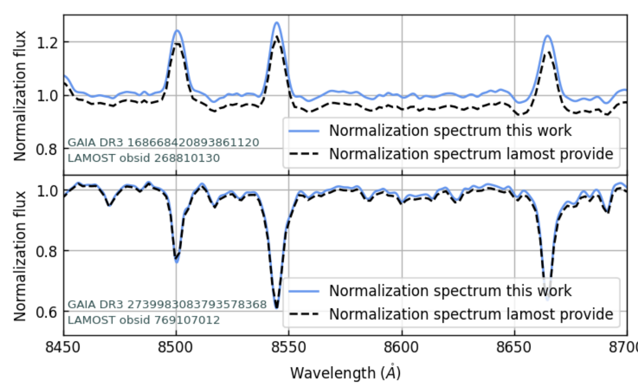

Figure 1. Comparison of different normalization methods in IRT bandpass. the upper panel is the emission lines spectrum and the lower is the absorption lines spectrum. The blue curve is the local normalized spectra by this work and the black curve is the global normalized spectra provided by LAMOST DR9.

3.2. *Templates*

For late-type stars. the dissipation of acoustic energy (Schrijver et al. 1989) and turbulent dynamo activity from non-rotating plasma (Bercik et al. 2005) in the upper photosphere contributes to the core of Ca II H&K and Ca II IRT lines. Therefore, it is better to subtract this "basal" flux from the spectrum to derive the true chromosphere activity. Andretta et al. (2005) investigated the non-local thermodynamic equilibrium (NLTE) effect on Ca II IRT lines, and found that the Central-Depression (CD) index can be affected by NLTE by more than 20%. Sinece our R^+ and R indices are defined on a narrow band of 1Å, similar to CD index, NLTE should be consider in R^+ index to remove the basal flux. The LTE `BT-Settl` spectral model and the NLTE model for Ca II lines (Allard et al. 2013) based on `Phoenix` (Husser et al. 2013) code were applied to subtract the basal flux in IRT bandpass.

The grids of `BT-Settl` templates are listed in Table 3. These templates were interpolated with intervals of $\Delta T_{eff} = 10K$, $\Delta \log\, g = 0.01$ and $\Delta[Fe/H] = 0.01$ to ensure a precise match with our observational spectra. The templates are degraded to $R \approx 1800$ and subtracted from the observed spectra, as equation 2.

Table 3. Parameter Space of The Grid

Parameter	Range	Grid Size
T_{eff}(K)	4800-6800	100
log g	3.5-5.0	0.5
$[Fe/H]$	[-1.0,-0.5,0,0.3,0.5]	-
$[\alpha/Fe]$	0.0-0.4	0.2

Note—For most LAMOST spectra in DR9, α abundance is not provided, the following empirical relations are employed to derive α abundance : $[Fe/H] = 0.0, +0.3, +0.5$ with $[\alpha/Fe] = 0.0$, $[Fe/H] = -0.5$ with $[\alpha/Fe] = +0.2$, $[Fe/H] = -1.0$ with $[\alpha/Fe] = +0.4$. (Khoperskov et al. 2021)

3.3. *Uncertainties Estimation*

Similar to the LAMOST Ca II H&K index error budget analysis in Zhang et al. (2022) , for Ca II IRT R index, we consider three factors of uncertainty as follows:

1. Uncertainty of spectral flux. LAMOST releases the target spectrum along with the corresponding spectrum of inverse variance($1/\delta^2$), which could be used to estimate the flux uncertainty:

$$\delta R_{flux} = \sqrt{\frac{1}{\lambda_2 - \lambda_1}\int_{\lambda_1}^{\lambda_2} (\frac{\delta(\lambda)}{C(\lambda)})^2 \, d\lambda}, \quad (3)$$

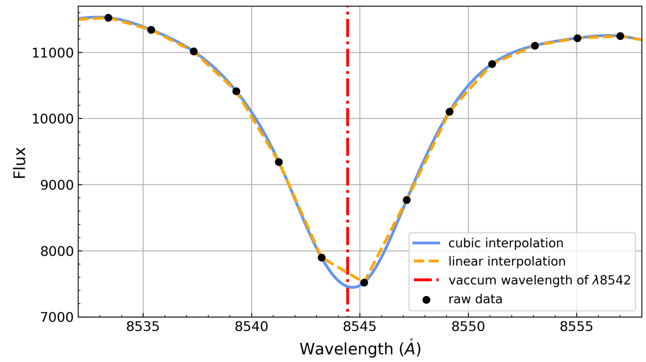

Figure 2. Difference of two interpolation methods. Black dots are observed spectrum; Blue curve is the cubic spline interpolation of the spectrum; Orange dash curve is the linear interpolation; Red dot-dash line shows the vaccum wavelength of λ8542.

where $C(\lambda)$ is the continuum, same as defined in equation 1.

2. Uncertainty of interpolation. As the wavelength intervals of LAMOST spectra is 2Å, the spectrum are interpolated. Different interpolation method lead to the uncertainty of R index, as illustrated in Figure 2. The uncertainty of interpolation is derived as:

$$\delta R_{interpolation} = |R_{cubic} - R_{linear}|, \quad (4)$$

to ensure that our choice of 1 Å window doesn't impact our conclusions, we compared the R indices of each Ca II IRT line measured in a 1 $\AA$ window with those of the 2 $\AA$ window. For majority of targets, the difference is negligible, as shown in Figure 3.

3. Uncertainty of red shift (or radial velocity). by using $z + z_{err}$, z, $z - z_{err}$ provided by LAMOST DR9, we can obtain R_+, R, R_- respectively for each line, so the δR_z is represented as following:

$$\delta R_z = \frac{|R - R_+| + |R - R_-|}{2}. \quad (5)$$

Combining function 3,4 and 5, the total uncertainty δR is give by:

$$\delta R = \sqrt{\delta R^2_{flux} + \delta R^2_{interpolation} + \delta R^2_z}. \quad (6)$$

For the R^+ index, the additional uncertainty comes from the templates. Utilizing the stellar parameter errors provided by LAMOST DR9, we calculated a series of R indices for each templates around the best template, $[T_{eff} \pm \Delta T$, $\log\, g \pm \Delta \log\, g$, $[Fe/H] \pm \Delta[Fe/H]]$.

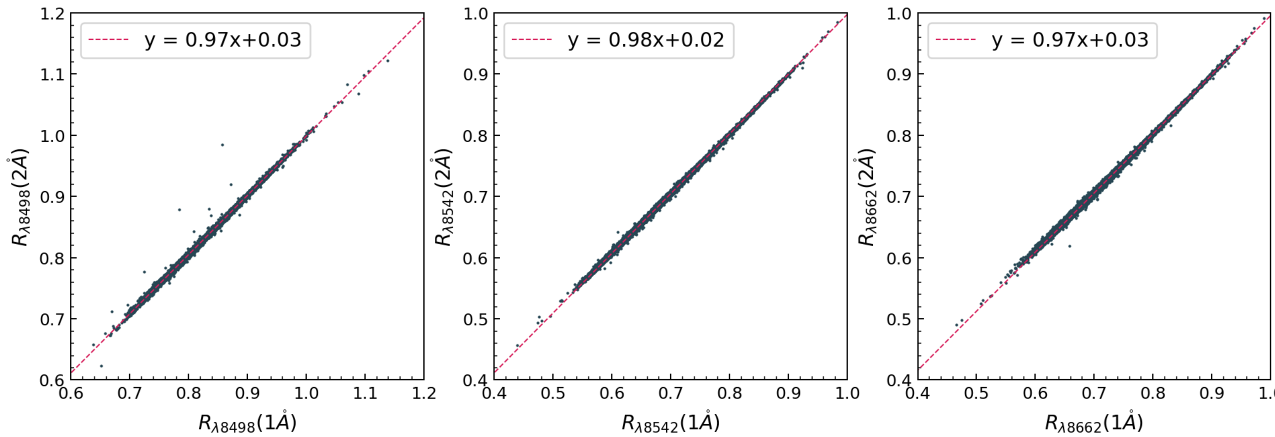

Figure 3. Comparison of R index derived from 1 $\AA$ and 2 $\AA$ widths respectively for each IRT line. Red dash line is obtained by least squares fitting of the data.

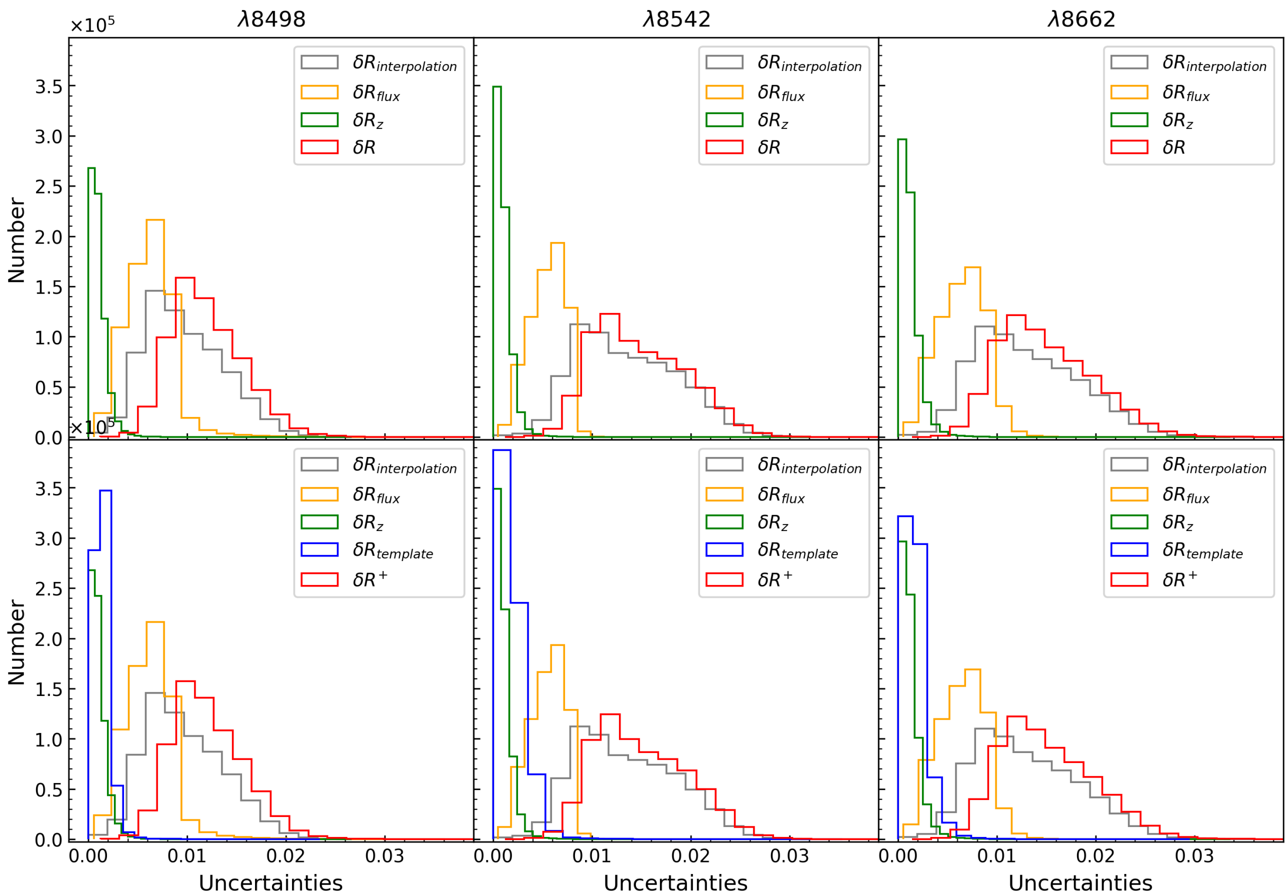

Figure 4. Distribution of uncertainties for the spectral lines $\lambda 8498$, $\lambda 8542$, and $\lambda 8662$ in three columns from left to right. Each column includes two panels, with the top one showing the distribution of uncertainty for R and its individual component, and the bottom one displaying the distribution of uncertainty for R^+, both represented by the red histogram.

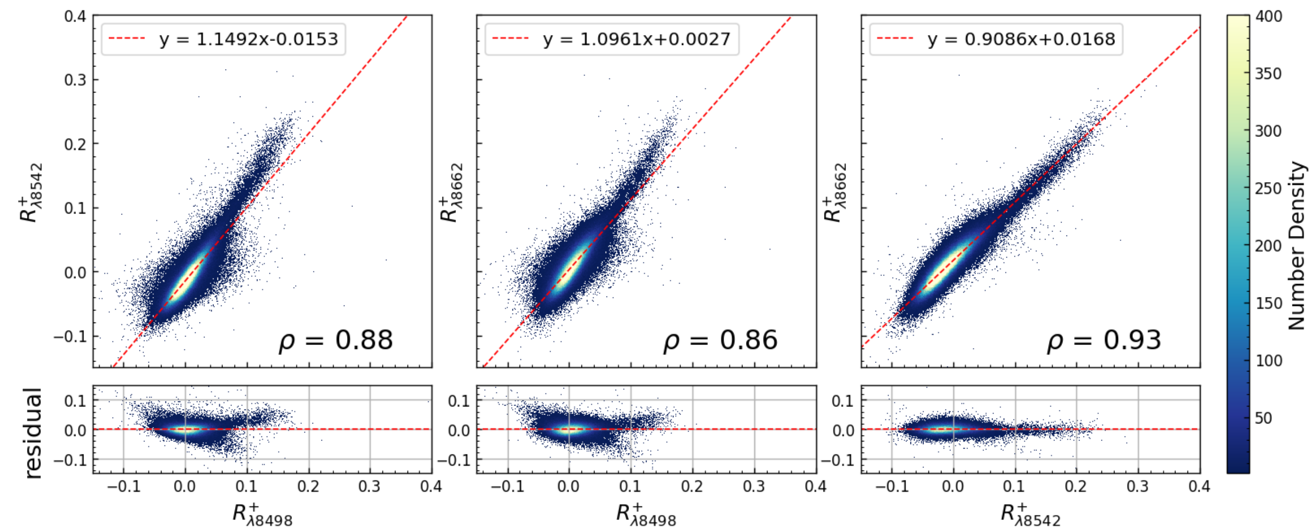

Figure 5. Linear regression is performed for each pair of R^+ values, with the corresponding residuals between the data and the fitted line shown in the lower panels. The left column displays $R^+_{\lambda 8498}$ - $R^+_{\lambda 8542}$, the middle column shows $R^+_{\lambda 8498}$ - $R^+_{\lambda 8662}$, and the right column depicts $R^+_{\lambda 8542}$ - $R^+_{\lambda 8662}$. The red dashed lines represent the regression equations obtained from fitting the data, while ρ corresponds to the Pearson correlation coefficient.

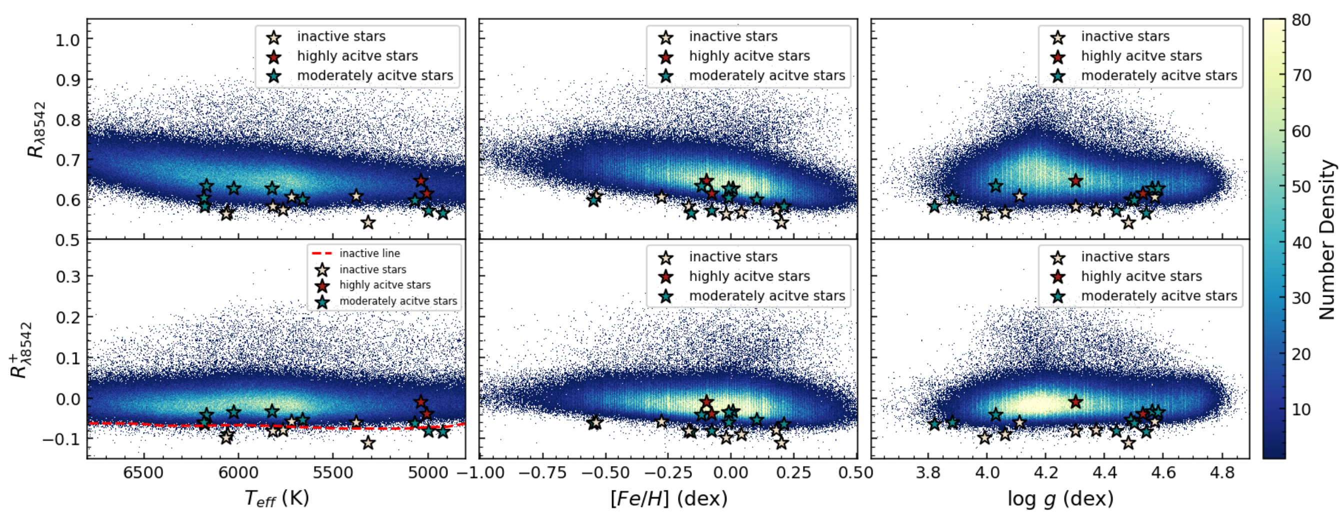

Figure 6. The distributions of $R_{\lambda 8542}$ and $R^+_{\lambda 8542}$ with stellar parameters. From left to right are T_{eff}, $[Fe/H]$ and log g, respectively. The upper section in each panel is for the R index and the lower are for R^+, as indicated in the plot.The red dashed line in the lower left panel is the lower 2σ line to selected inactive star in Figure.8. Stars symbols are bright stars with well studied activity in Baliunas et al. (1995) and Hall et al. (2007, 2009). Spectra are extracted from ESO archive. Inactive stars: HD1461, HD3795, HD9562, HD45067, HD126053, HD187691, HD197076; Moderately active stars: HD16160, HD16673, HD20630, HD30495, HD35296, HD39587, HD88873, HD155885, HD160346; Highly active stars: HD17925, HD22049. See text for details.

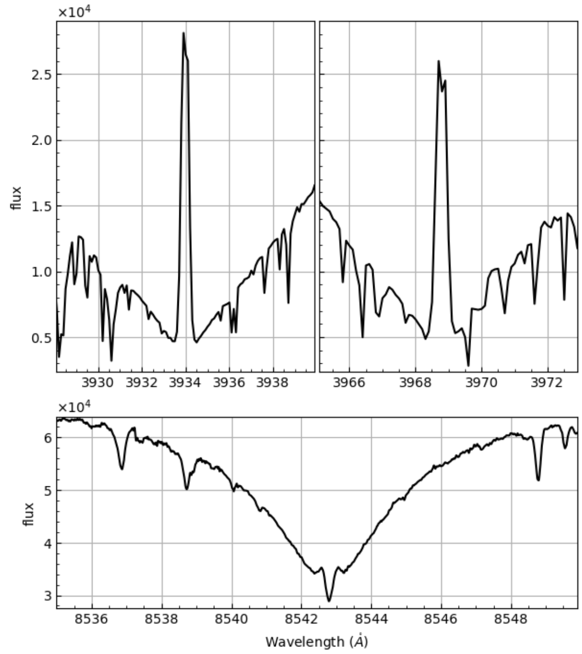

Figure 7. High resolution spectrum of HD 22049. Top left: Ca II K; Top right: Ca II H; Lower: Ca II $\lambda8542$

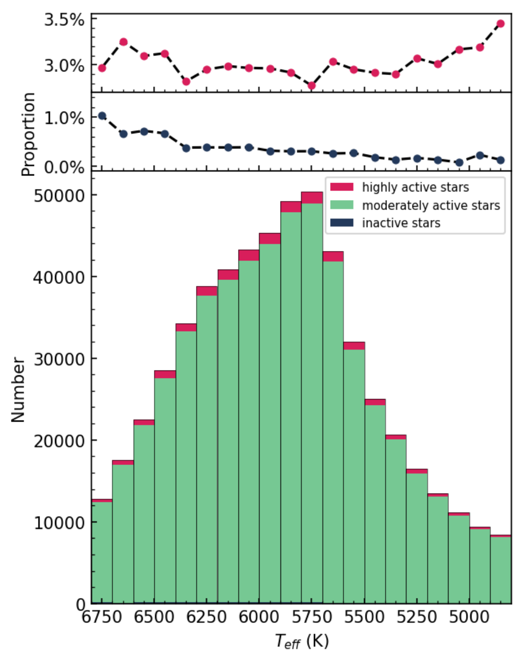

Figure 8. Top and middle panels show the proportion of high active and inactive stars, respectively. The bottom panel shows the number count of different category in different temperature bins, as indicated by different color.

The maximum and minimum of the template index R_T are denoted as R_T^{max} and R_T^{min} respectively. The uncertainty of the template index R_T is then calculated as:

$$\delta R_T = max(|R_T - R_T^{max}|,\ |R_T - R_T^{min}|), \quad (7)$$

and the uncertainty of R^+ is given by:

$$\delta R^+ = \sqrt{\delta R^2 + \delta R_T^2}. \quad (8)$$

Figure 4 illustrates the contribution of different components to δR and δR^+. It can be observed that the uncertainty of R^+ is mainly dominated by interpolation and flux error.

Table 4. Columns of Catalog

Column	Unit	Description
obsid		LAMOST observation identifier
gaia_source_id		Source identifier in Gaia DR3
gaia_g_mean_mag		G mag provided by Gaia DR3
snri		SNR at i band
snrz		SNR at z band
ra_obs	degree	RA of fiber point
dec_obs	degree	DEC of fiber point
teff	K	T_{eff}, Effective temperature
teff_err	K	Uncertainty of T_{eff}
logg	dex	log g, Surface gravity
logg_err	dex	Uncertainty of log g
feh	dex	$[Fe/H]$, Metallicity
feh_err	dex	Uncertainty of $[Fe/H]$
rv	km/s	V_r, Radial velocity
rv_err	km/s	Uncertainty of V_r
R_8498		$R_{\lambda8498}$
R_8498_err		uncertainty of $R_{\lambda8498}$
R_8542		$R_{\lambda8542}$
R_8542_err		uncertainty of $R_{\lambda8542}$
R_8662		$R_{\lambda8662}$
R_8662_err		uncertainty of $R_{\lambda8662}$
R_plus_8498		$R^+_{\lambda8498}$
R_plus_8498_err		uncertainty of $R^+_{\lambda8498}$
R_plus_8542		$R^+_{\lambda8542}$
R_plus_8542_err		uncertainty of $R^+_{\lambda8542}$
R_plus_8662		$R^+_{\lambda8662}$
R_plus_8662_err		uncertainty of $R^+_{\lambda8662}$

NOTE—If some of the stellar parameter errors or the index errors are not available in the data release, the corresponding error values in the table are filled with -9999.

4. STELLAR ACTIVITY DATABASE

We calulated the R and R^+ indices and their corresponding errors for 699,348 F, G and K-type spectra selected from LAMOST DR9 database. The result are written in a CSV table and uploaded to the website https://www.doi.org/10.12149/101245. The column descriptions of the database can be found in Table 4. Our R and R^+ index database can be used as an indicator for stellar activity studies.

Theoretically, the R^+ index should be close to zero for inactive stars, but there is a significant fraction of stars with R^+ values below zero (see Figure 6). Similar negative values are also found in GAIA (Lanzafame et al. 2023) and RAVE (Žerjal et al. 2013) Ca II IRT index measurements. We believe that the following reasons may have contributed to this:

1. The parameters of LAMOST spectra may not have been measured accurately.
2. Low or moderate chromospheric activity could produce some extra absorption (Mullan 1979; Lanzafame et al. 2023).

5. DISCUSSION

5.1. *Relationship between IRT indices and stellar parameters*

In Figure 5, we plotted the Ca II IRT R^+ against each other. There are clear linear correlations in all plots. We calculated the Pearson correlation coefficient and marked at the lower part of each panel. For each pair, the ridge of the density distribution is fitted with a linear function using the `Bayesian Ridge Regression` algorithm from the `sklearn` module (Pedregosa et al. 2011). The functions are shown on the top of each panel in Figure 5. From the figure, we can see that $R^+_{\lambda 8542}$ vs. $R^+_{\lambda 8662}$ exhibit the strongest linear relationship, with a higher Pearson coefficient than other pairs. The λ8542 line is the most opaque member of the Ca II IRT lines and usually considered as a better diagnostic for chromospheric activities (Linsky et al. 1979b). Based on the linear function slopes, the strength of $R^+_{\lambda 8542}$ is greater than the other two lines, our results confirms the conclusion of Linsky et al. (1979b) and are also consistent with the findings of Žerjal et al. (2013) and Martin et al. (2017). Henceforth, we limit our discussion to λ8542, although all the other line indices are available in our database for possible use.

The distributions of $R^+_{\lambda 8542}$ and $R_{\lambda 8542}$ with stellar parameters are presented in Figure 6. As could be noticed, there is a native bias in the R^+ index plot. The R^+ index is measured in a narrow band(1Å) around the line core. As pointed out in Linsky et al. (1979b), for chromoshpere quiet stars, even when the stellar parameters are the same, different turbulence, rotation or possible other parameter could lead to the uncertainty in the observed line profile. Also, the released LAMOST stellar parameters are measured in the blue part of the spectra, the theoretical stellar template may possibly not fully fit the observed near infrared lines, especially in the narrow line core, further more, the stellar activity may also bias the stellar parameter measurement. So we suspect the mismatch between the template and the observed line core may cause the negative bias, but the relative R^+ index may still reflect the stellar activity. To test the reliability of our R^+ index, we applied our method to the well studied nearby northern field stars listed in Baliunas et al. (1995) and Hall et al. (2007, 2009). Those stars are confirmed as active or inactive by both Ca II H&K time and photometric time series. As those stars are too bright for LAMOST surveys, we accessed the high-quality spectra of these stars from ESO archive[1], and find 18 stars with available data in both Ca II H&K and IRT band. The spectra were degraded to LAMOST resolution and the R and R^+ indices of those stars are presented in Figure 6. The S index vs the R^+ index of these stars are also plotted in Figure 13. The inactive, moderately active and high active stars are shown by different color in Figure 6, their relative position in the plot are consistent with their defined activity. However, the moderately and highly active stars don't show higher R^+ index in the plot, this is not uncommon in the active stars defined by Ca II H&K lines, as Ca II IRT lines don't have to show emission cores as strong as H&K lines (Linsky et al. 1979b). As an example, in Figure 7, we plot the spectrum in both the Ca II H&K and IRT bands for ones of the high active star in the sample, HD 22049, with average S index $\langle S \rangle$=0.46 (Baliunas et al. 1995). The high resolution spectra show strong emission core in the H&K lines, while it's much less evident in the case of λ8542. The tiny bump will be smeared in the low LAMOST resolution spectra. So it reasonable that the HD 22049 don't show strong activity in $R^+_{\lambda 8542}$ index.

Stars with low activity are also important for low-mass exoplanets studies, since life may more possibly exist in a planet hosted by low-active star, and exoplanets may be more easily discovered around low-active stars than active because both the observed lightcurve and radial velocity curve will be more stable due to less spots on the star (e.g. Korhonen et al. 2015; Hojjatpanah et al.

[1] https://archive.eso.org/

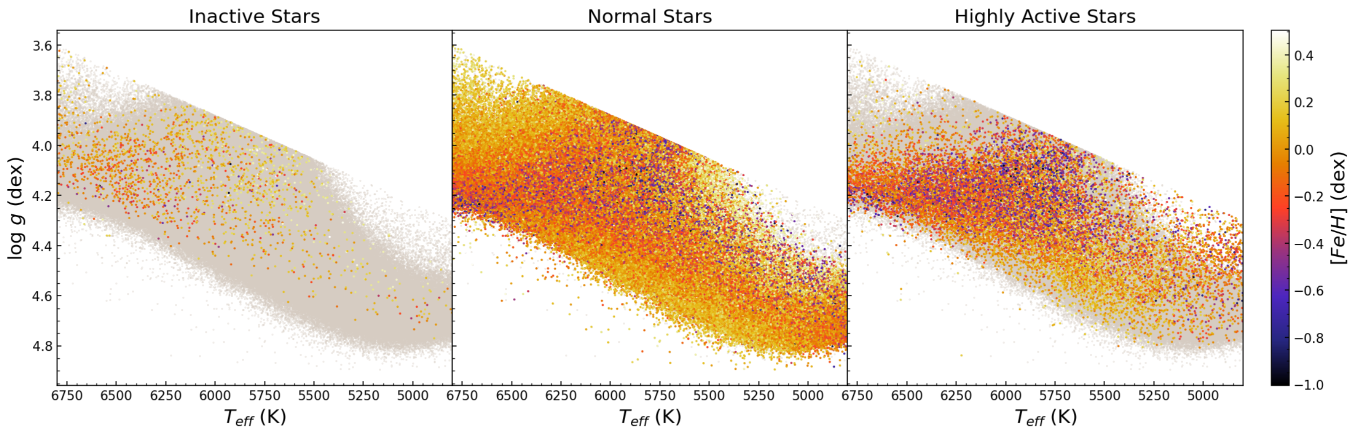

Figure 9. Distribution of inactive, normal and high active stars in the T_{eff} and $Logg$ space, different color represent different [Fe/H], as indicated by the color bar.

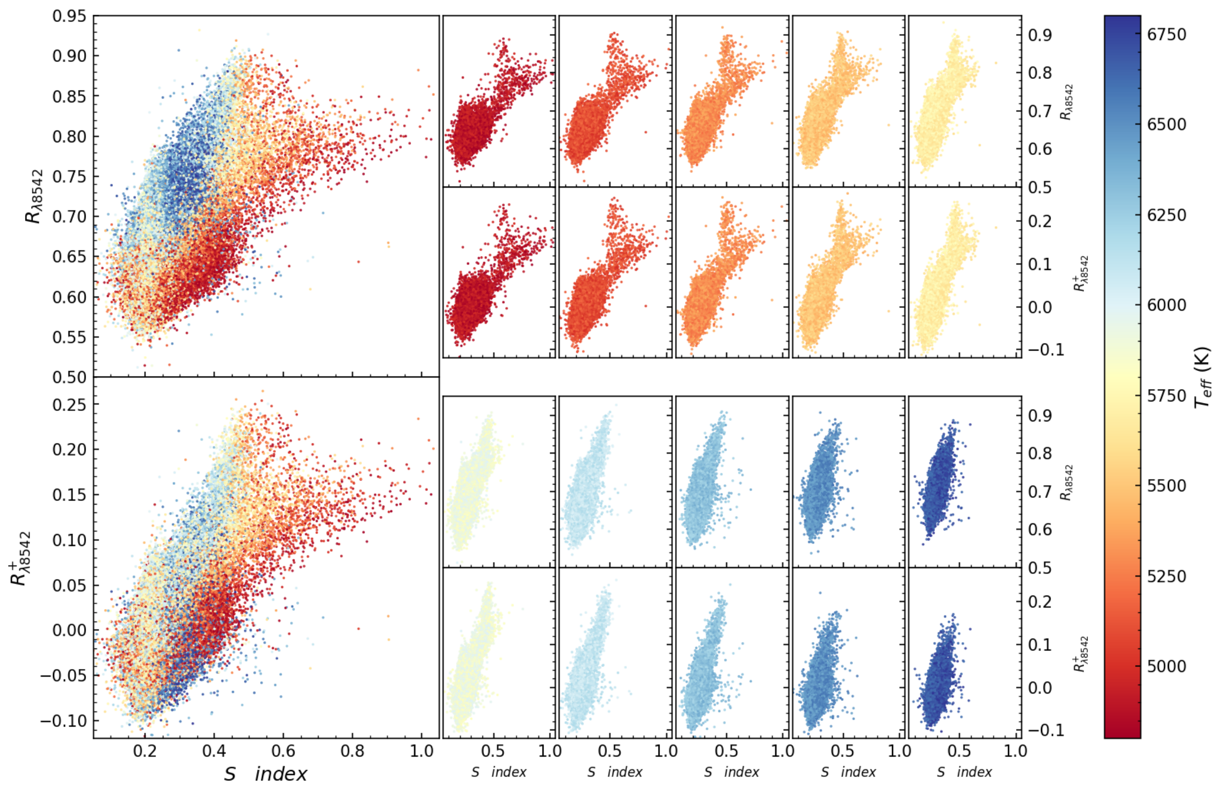

Figure 10. Left top panel shows the relationship between the S index and $R_{\lambda 8542}$, while the left bottom panel illustrates the relationship of S index and $R^{+}_{\lambda 8542}$. The colors of each point represent their temperature, as indicated by the color bar. To make a clear view of how the indices distribution changes with the temperature, small panels on the right side show similar indices distribution as the left panels, but with T_{eff} range limited to 200K.

2020). To take a peek at the distribution of the chromospheric active and inactive stars, the star are divided into 20 temperature bins, and the number count in each bins are plotted in the bottom panel of Figure 8. The mean and variance of $R^+_{\lambda8542}$ are calculated for each bin. Stars with R^+ index higher than 2σ are defined as high-active stars and those lower than 2σ are inactive stars. The fractions of active and inactive stars are plotted in the upper 2 panels of Figure 8. The fraction of inactive stars decreases with temperature. While the fraction of active stars increases with the decreasing temperature below 5800K and increases with temperature above 5800K. As there is a large fraction of high R^+ index stars are actually binaries (see Section 5.2 below), the increasing fraction of active stars with temperature may reflect the increasing binary fraction with mass rather than the increasing activity. Further work is needed to clarify this.

The distributions of highly active, inactive and moderatly active stars in the stellar parameter space are shown in Figure 9. The inactive stars exhibit high metallicity in Figure 9 , indicating that they are thin disk population, similarly, the low metallicity population in the active stars plot may possibly comes from the local thick disk population. As some stars were observed several times by LAMOST, for Figure 6, 8 and 9, only one spectrum were kept for stars with multiple visits to ensure the fraction is not biased by repeat count. As the stellar activity is a complicated function of mass, age, metallicity and rotation, which is beyond the scope of the current paper, we will leave the detailed analysis for future work.

5.2. *Comparing with S index*

Comparing our database with Ca II *H&K* *S* index of Zhang et al. (2022), there are 0.58 million spectra in common(Table 1). The *S* index vs. $R^+_{\lambda8542}$ and *S* index vs. $R_{\lambda8542}$ are plotted in Figure 10. Both plots show a linear relation between *S* index and $\lambda8542$ indices, with R^+ being less scattered than the *R* index, as the basal photospheric contribution was removed. In Figure 10, we also plotted the *S* index vs. R^+ and *R* index with T_{eff} in every 200K bins. It shows that as the temperature decreases, the relationship between *S* and $R^{(+)}$ index becomes increasingly nonlinear. Visually inspecting Figure 10, the high-activity index star seems to be divided into 3 branches. We label the 3 branches in Figure 11 and plot their distributions in stellar parameter space in the lower panels of Figure 11 respectively. For Branch 1, we did not find any specific tendencies in the distribution of T_{eff} and $[Fe/H]$, but they almost located at log $g < 4.5$. Branch 2 has a lower R^+ index than Branch 1 and extends to a very high *S* index end. They are distributed at temperatures below 5750K and exhibits high metallicity. Branch 3 has high *S* index but low $R^+_{\lambda8542}$ index. The sample size of Branch 3 is small, but they has a broad temperature range. They shows high metallicity in the low-temperature end and low metallicity in the high temperature end.

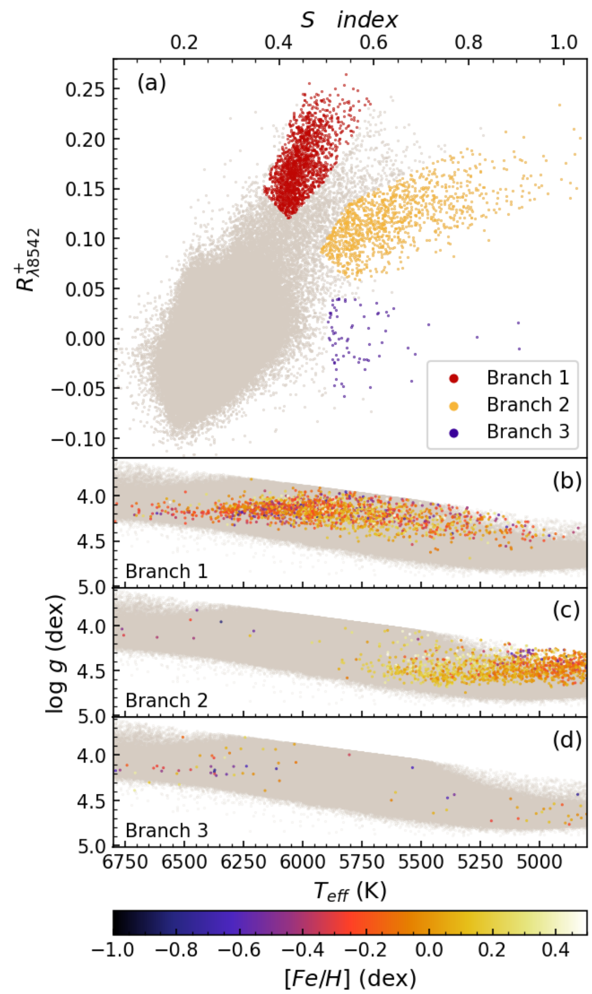

Figure 11. (a): Distribution of *S* - $R^+_{\lambda8542}$, different branches are defined by eyes and plotted in different colors,as indicated in the frame. The background stars are shown in grey. (b): Distribution of Branch 1 stars in stellar parameter space. Metallicity is indicated by color, as shown in the bottom color bar, (c): Distribution of Branch 2 stars. (d): Distribution of Branch 3 stars.

To investigate the properties of the 3 groups, we checked the spectra by eyes, and the typical spectra are show in Figure 12.

1. Most of the spectra in Branch 1 show the characteristic double lines at the IRT bandpass and H&K lines are broader than the template, which is typical in spectral binaries. For LAMOST LRS,

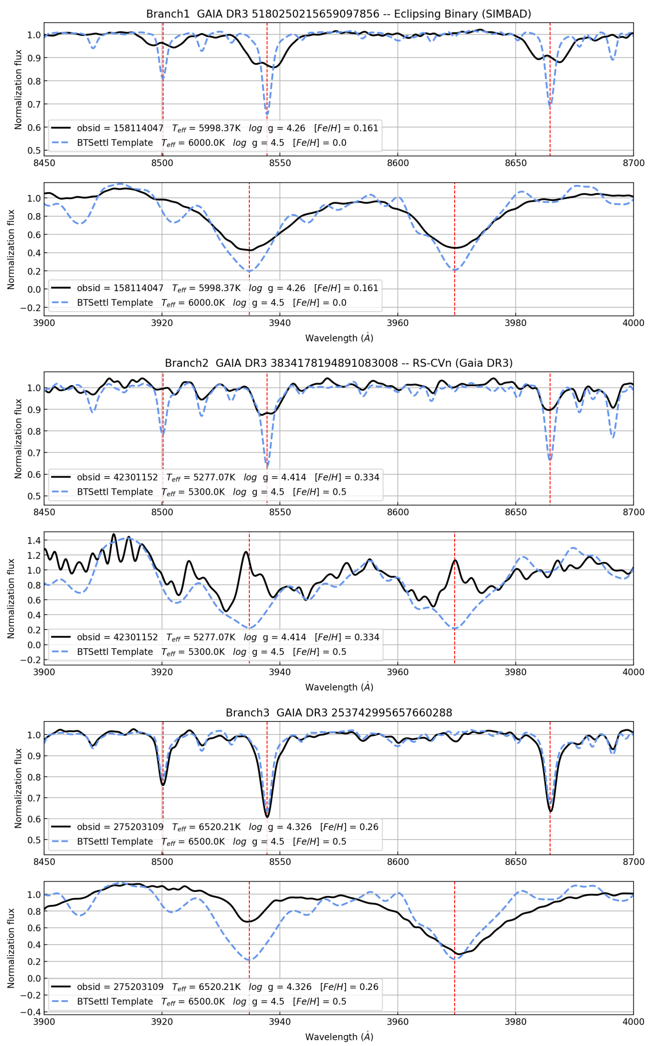

Figure 12. The typical spectra from the 3 branch stars are shown in Figure 11. From top to bottom are a star of Branch 1,2 and 3 respectively. The spectra and the corresponding templates of the Ca II IRT region and the Ca II H&K region are plotted respectively.

the radial velocity separation should be more than 150km/s for the 2 lines to be clearly discerned. Therefore, those are highly possible to be close binaries with a larger RV difference and similar luminosity. To confirm this conclusion, we cross-matched the `gaiadr3.vari_eclipsing_binary` catalog (Gaia et al. 2016; Vallenari et al. 2023; Mowlavi et al. 2023), which yielded 1727 common spectra (1507 common sources). About 66% (997/1507) of stars in our defined Branch 1 region (see Figure 11) coincide with the *Gaia* dr3 eclipsing binaries. As the *Gaia* samples are selected by light curves thus are highly dependent on the inclination angle, the rest 34% of Branch 1 may consist of either spectral binaries with low inclination

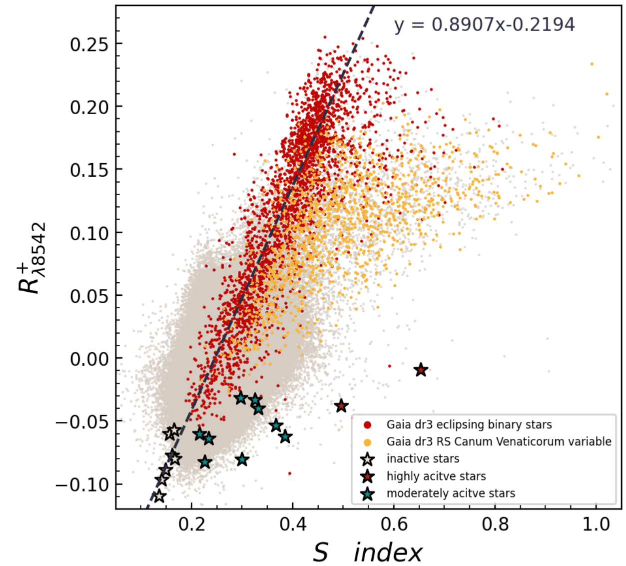

Figure 13. $R^+_{\lambda 8542}$ vs. S index distribution. The background grey points are the same as Figure 10. Overlaid color samples are stars cross matched with gaia dr3 eclipsing binaries and RS-CVn variables, respectively. As indicated in the plot, these two samples are coincide with Brach 1 and Brach 2 defined in Figure 11, respectively. The black dash line is the linear regression of the eclipsing binary sample, function is given. Star symbols are the same as in Figure 6

that show no eclipse in lightcurve, or possibly some single stars show real high activity. Therefore, a large fraction of this branch should be close binaries mimic the chromospheric emission due to the index calculation algorithm, most of them are not active stars, or at least not as high as the S or R index indicated. Further investigation is necessary to determine their nature. The *Gaia* eclipsing binary samples extend linearly to the low-active index end in the S vs. R^+ plot (see Figure 13). We fitted the *Gaia* samples with RANSAC (Random Sample Consensus) regression algorithm provided by `sklearn` package (Pedregosa et al. 2011), the result is shown in Figure 13.

2. For Branch 2, we observed obvious emission cores in most of the spectra at the H&K lines, and filled-in cores of the Ca II IRT absorption lines. So the branch 2 is dominated by highly chromospheric activity stars. From the parameters distribution, they are predominantly metal-rich (i.e. $[Fe/H] > -0.2$) cool stars ($T_{eff} < 5700K$). As RS Canum Venaticorum variables (RS-CVn) are a type of chromospheric active binaries, we cross-correlated our catalog with the *Gaia* RS-CVn catalog (Rimoldini et al. 2023), and obtained 1187

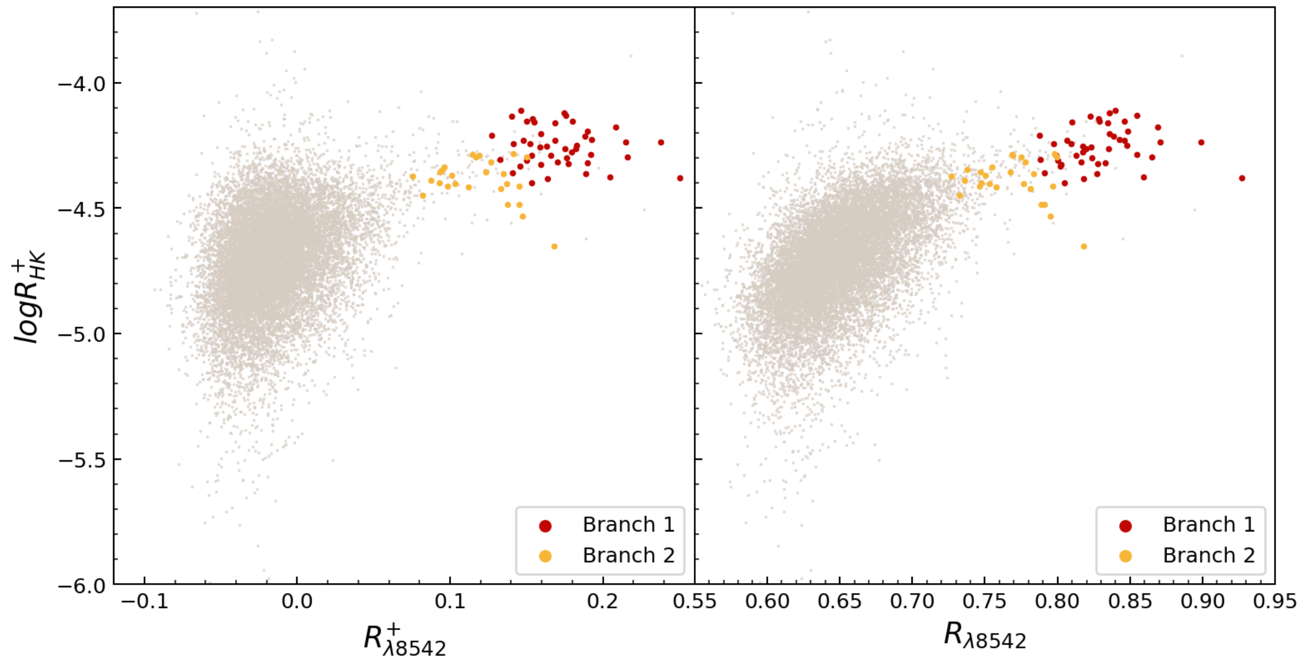

Figure 14. Left panel: Relationship of $R^+_{\lambda8542}$ vs. $logR^+_{HK}$. Right panel: Relationship of $R_{\lambda8542}$ vs. $logR^+_{HK}$. Red and yellow points represent stars from Branch 1 and 2 as defined in 11, respectively.

spectra (1037 stars) in common. The matched *Gaia* RS-CVns are plotted in Figure 13, and most of these stars are consistent with Branch 2 and exhibit clear difference from eclipsing binaries.

3. Branch 3 shows a higher S index and a relatively lower R^+ index, which means the H&K lines exhibit higher activity than IRT lines. We suspect this may be caused by binaries or visually close stars with different temperatures, where the blue and red region are dominated by different star falling into the same fiber. Since there are only 70 stars in this category, these stars were checked one by one. Miscellaneous information such as CDS (http://cdsportal.u-strasbg.fr/) images, SED, LAMOST spectra, *Gaia* `non-single star` list (Holl et al. 2023), TESS light curves (Ricker et al. 2015; Sullivan et al. 2015) and Kepler light curves (Howell et al. 2014) were collected to help to understand the nature of these targets, and this information is listed in the last column of Table A1. From the table, 21 of them are binaries or spacial coincidences, supporting our speculation. 27 of them are variables that may show high activity, 10 of them have no particular reason and the rest of them are due to pollution or are with wrong spectral type. Further study is necessary to know their nature.

5.3. *Comparing with R^+_{HK} index*

Using the $logR^+_{HK}$ index in Zhang et al. (2020) (Table 1), the distribution of $R^+_{\lambda8542}$ vs. $logR^+_{HK}$ and $R_{\lambda8542}$ vs. $logR^+_{HK}$ are plotted in Figure 14. The stars in Branch 1 and Branch 2 in the previous section are also plotted. The overall distribution is similar to Žerjal et al. (see 2013, Fig.7), though they used EW_{IRT} as an infrared activity indicator. Binary stars are more likely to appear in the region of both high H&K and high IRT index, similar to Žerjal et al. (2013). From Fig 13 and 14, high H&K or high IRT index alone is not a good indicator of activity, as there is a large population of binaries with low stellar activity mimic the high activity star. Combing the H&K index and the IRT index, especially in the S vs. $R^+_{\lambda8542}$ distribution plot, will be more helpful to discern different populations of stellar activity.

6. CONCLUSION

We defined new near-infrared Ca II triplet stellar activity indices, R and R^+, and derived the indices for 699,348 spectra of 562,863 solar like F, G and K-type stars. These activity indices, as well as their estimated uncertainties and other basic information are integrated in a database available at https://www.doi.org/10.12149/101245.

Comparing the indices of $\lambda8498$, $\lambda8542$ and $\lambda8662$ lines, they show linear correlation within each pair. The $R^+_{\lambda8542}$ is the strongest among the three lines, and could be used as the indicator to represent the Ca II IRT activity. We presented the distribution of λ8542 index in stellar parameter space, and selected samples of high-active and low-active stars, respectively. The fraction of low-active stars decrease with the temperature, while the fraction of high-ctive stars first decrease with the temperature above 5800K, then below 5800K, the fraction increases with decreasing temperature. We further compared our infrared activity index with the Ca II H&K index and found that the high S index star could be divided into 3 branches, Branch 1 are mostly spectral binaries with double lines that mimic the emission line core, Branch 2 comprises RS-CVns showing high activity, and Brach 3 includes stars with a high S index but relatively low $R^{+}_{\lambda 8542}$ index due to difference reasons. Combining the CaII H&K S index and $R^{+}_{\lambda 8542}$ is particularly useful in selecting true chromospheric active stars. Future work is necessary to exclude contamination from low-active binaries and establish a pure sample of high-active stars.

ACKNOWLEDGEMENTS

This work is supported by the National Key R&D Program of China 2019YFA0405000 and NSFC 12273056. Z.H.T. also thanks the support of the National Key R&D Program of China 2022YFA1603002, NSFC 12090041, NSFC 11933004 and NSFC 12273056.

This work has made use of data from the Guoshoujing Telescope(the Large Sky Area Multi-Object Fiber Spectroscopic Telescope, LAMOST). LAMOST is operated and managed by the National Astronomical Observatories, Chinese Academy of Sciences. (http://www.lamost.org/public/?locale=en). Funding for the LAMOST has been provided by the National Development and Reform Commission.

This work has made use of data from the European Space Agency (ESA) mission *Gaia* (https://www.cosmos.esa.int/gaia), processed by the *Gaia* Data Processing and Analysis Consortium (DPAC, https://www.cosmos.esa.int/web/gaia/dpac/consortium). Funding for the DPAC has been provided by national institutions, in particular the institutions participating in the *Gaia* Multilateral Agreement.

This research has made use of the SIMBAD database, operated at CDS, Strasbourg, France.

This paper includes data collected by the Kepler mission and obtained from the MAST data archive at the Space Telescope Science Institute (STScI). Funding for the Kepler mission is provided by the NASA Science Mission Directorate. STScI is operated by the Association of Universities for Research in Astronomy, Inc., under NASA contract NAS 5–26555.

This paper includes data collected with the TESS mission, obtained from the MAST data archive at the Space Telescope Science Institute (STScI). Funding for the TESS mission is provided by the NASA Explorer Program. STScI is operated by the Association of Universities for Research in Astronomy, Inc., under NASA contract NAS 5–26555.

The HD stellar spectra we used in Section 5.1 based on data obtained from the ESO Science Archive Facility with DOI(s):

- https://doi.org/10.18727/archive/24,
- https://doi.org/10.18727/archive/50,
- https://doi.org/10.18727/archive/71,
- https://doi.org/10.18727/archive/72,

Facilities: LAMOST, GAIA, TESS, Kepler

Software: Astropy (Robitaille et al. 2013; Price-Whelan et al. 2018, 2022), Astroquery (Ginsburg et al. 2019), SciPy (Virtanen et al. 2020), NumPy (Harris et al. 2020), Scikit-learn (Pedregosa et al. 2011), Matplolib (Hunter 2007), TOPCAT (Taylor 2005), Lightkurve (Lightkurve Collaboration et al. 2018; Brasseur et al. 2019)

REFERENCES

Allard, F., Hauschildt, P. H., Alexander, D. R., & Starrfield, S. 1997, ARA&A, 35, 137

Allard, F., Homeier, D., & Freytag, B. 2011, in 16th Cambridge Workshop on Cool Stars, Stellar Systems, and the Sun, Vol. 448, 91

Allard, F., Homeier, D., Freytag, B., Schaffenberger, W., & Rajpurohit, A. 2013, Memorie della Societa Astronomica Italiana Supplementi, 24, 128

Andretta, V., Busà, I., Gomez, M., & Terranegra, L. 2005, A&A, 430, 669

Bai, Z.-R., Zhang, H.-T., Yuan, H.-L., et al. 2017, Research in Astronomy and Astrophysics, 17, 091

—. 2021, Research in Astronomy and Astrophysics, 21, 249

Baliunas, S. L., Donahue, R. A., Soon, W. H., et al. 1995, ApJ, 438, 269, doi: 10.1086/175072

Bercik, D., Fisher, G., Johns-Krull, C., & Abbett, W. 2005, ApJ, 631, 529

Brasseur, C., Phillip, C., Fleming, S. W., Mullally, S., & White, R. L. 2019, Astrophysics Source Code Library, ascl

Cauzzi, G., Reardon, K., Uitenbroek, H., et al. 2008, A&A, 480, 515

Cincunegui, C., Diaz, R. F., & Mauas, P. J. D. 2007, A&A, 469, 309

de Grijs, R., & Kamath, D. 2021, Universe, 7, 440

Gaia, C., Bono, G., et al. 2016, A&A, 595, 1

Gentile Fusillo, N., Rebassa-Mansergas, A., Gänsicke, B., et al. 2015, MNRAS, 452, 765

Ginsburg, A., Sipőcz, B. M., Brasseur, C. E., et al. 2019, AJ, 157, 98, doi: 10.3847/1538-3881/aafc33

Hall, J. C., Henry, G. W., Lockwood, G. W., Skiff, B. A., & Saar, S. H. 2009, AJ, 138, 312, doi: 10.1088/0004-6256/138/1/312

Hall, J. C., Lockwood, G. W., & Skiff, B. A. 2007, AJ, 133, 862, doi: 10.1086/510356

Harris, C. R., Millman, K. J., van der Walt, S. J., et al. 2020, Nature, 585, 357, doi: 10.1038/s41586-020-2649-2

He, H., Zhang, W., Zhang, H., et al. 2023, Ap&SS, 368, 63

Hojjatpanah, S., Oshagh, M., Figueira, P., Santos, N., & Amazo-Gómez, E. 2020, A&A, 439, A35

Holl, B., Sozzetti, A., Sahlmann, J., et al. 2023, A&A, 674, A10, doi: 10.1051/0004-6361/202244161

Howard, W. S., Tilley, M. A., Corbett, H., et al. 2018, ApJL, 860, L30

Howell, S. B., Sobeck, C., Haas, M., et al. 2014, PASP, 126, 398

Hunter, J. D. 2007, Computing in Science & Engineering, 9, 90, doi: 10.1109/MCSE.2007.55

Husser, T.-O., Wende-von Berg, S., Dreizler, S., et al. 2013, A&A, 553, A6

Karoff, C., Knudsen, M. F., De Cat, P., et al. 2016, Nature Communications, 7, 11058

Khoperskov, S., Haywood, M., Snaith, O., et al. 2021, MNRAS, 501, 5176, doi: 10.1093/mnras/staa3996

Korhonen, H., Andersen, J., Piskunov, N., Hackman, T., & Juncher, D. 2015, MNRAS, 448, 3038

Lanzafame, A. C., Brugaletta, E., Frémat, Y., et al. 2023, A&A, 674, A30, doi: 10.1051/0004-6361/202244156

Lightkurve Collaboration, Cardoso, J. V. d. M., Hedges, C., et al. 2018, Lightkurve: Kepler and TESS time series analysis in Python, Astrophysics Source Code Library. http://ascl.net/1812.013

Lillo-Box, J., Santos, N., Santerne, A., et al. 2022, A&A, 667, A102

Linsky, J. L., Hunten, D. M., Sowell, R., Glackin, D. L., & Kelch, W. L. 1979b, ApJS, 41, 481

Linsky, J. L., Worden, S., McClintock, W., & Robertson, R. M. 1979a, ApJS, 41, 47

Martin, J., Fuhrmeister, B., Mittag, M., et al. 2017, A&A, 605, A113

Mittag, M., Schmitt, J., Metcalfe, T., Hempelmann, A., & Schröder, K.-P. 2019, A&A, 628, A107

Mittag, M., Schmitt, J., & Schröder, K.-P. 2013, A&A, 549, A117

Mowlavi, N., Holl, B., Lecoeur-Taïbi, I., et al. 2023, A&A, 674, A16

Mullan, D. 1979, ApJ, 234, 579

Notsu, Y., Honda, S., Maehara, H., et al. 2015, PASJ, 67, 33

Pedregosa, F., Varoquaux, G., Gramfort, A., et al. 2011, Journal of Machine Learning Research, 12, 2825

Price-Whelan, A. M., Sipőcz, B., Günther, H., et al. 2018, AJ, 156, 123

Price-Whelan, A. M., Lim, P. L., Earl, N., et al. 2022, ApJ, 935, 167

Ren, J.-J., Raddi, R., Rebassa-Mansergas, A., et al. 2020, ApJ, 905, 38

Ricker, G. R., Winn, J. N., Vanderspek, R., et al. 2015, Journal of Astronomical Telescopes, Instruments, and Systems, 1, 014003

Rimoldini, L., Holl, B., Gavras, P., et al. 2023, A&A, 674, A14

Robitaille, T. P., Tollerud, E. J., Greenfield, P., et al. 2013, A&A, 558, A33

Schrijver, C. J., Cote, J., Zwaan, C., & Saar, S. H. 1989, ApJ, 337, 964

Shields, A. L., Ballard, S., & Johnson, J. A. 2016, PhR, 663, 1

Sullivan, P. W., Winn, J. N., Berta-Thompson, Z. K., et al. 2015, ApJ, 809, 77

Taylor, M. B. 2005, in Astronomical Society of the Pacific Conference Series, Vol. 347, Astronomical Data Analysis Software and Systems XIV, ed. P. Shopbell, M. Britton, & R. Ebert, 29

Tennyson, J. 2019, Astronomical Spectroscopy: An Introduction to the Atomic and Molecular Physics of Astronomical Spectroscopy (World Scientific)

Vallenari, A., Brown, A., Prusti, T., et al. 2023, Astronomy & Astrophysics, 674, A1

Virtanen, P., Gommers, R., Oliphant, T. E., et al. 2020, Nature Methods, 17, 261, doi: 10.1038/s41592-019-0686-2

Wilson, O. 1968, ApJ, 153, 221

Wright, J. 2005, PASP, 117, 657

Wu, Y., Luo, A.-L., Li, H.-N., et al. 2011, Research in Astronomy and Astrophysics, 11, 924

Žerjal, M., Zwitter, T., Matijevič, G., et al. 2013, ApJ, 776, 127

Zhang, J., Zhao, J., Oswalt, T. D., et al. 2019, ApJ, 887, 84

Zhang, J., Bi, S., Li, Y., et al. 2020, ApJS, 247, 9

Zhang, W., Zhang, J., He, H., et al. 2022, ApJS, 263, 12

Zhao, G., Zhao, Y.-H., Chu, Y.-Q., Jing, Y.-P., & Deng, L.-C. 2012, Research in Astronomy and Astrophysics, 12, 723

APPENDIX

A. LIST OF BRANCH 3 STARS

Table A1. Information of stars in Branch3

No.	obsid	gaia_source_id	g_mag	ra_obs	dec_obs	R^{+}_{8542}	S	Class
1	181415234	2742433723412879360	13.07488	1.883999	5.700471	0.0231	0.6297	*UV excess/binary?
2	255415044	390549008386598016	14.26488	11.21287	48.28147	0.0352	0.6049	*Bright Star Pollution
3	182715182	376725089206420864	14.22984	16.69563	44.43003	0.0131	0.5548	Variable (G)
4	209103032	114150201980200960	12.09423	40.99757	24.91994	-0.0209	0.5851	*Nearby Star Pollution
5	162403203	108894639478505472	13.62411	46.7181	22.2539	0.0155	0.9036	*Young Stellar Object Candidate
6	157302145	125962495916228992	12.85282	50.73753	34.37201	-0.0040	0.6170	Variable(G)
7	286103110	67691055407537792	13.16509	53.43127	23.15588	-0.0176	0.6104	Binary (G)
8	307915107	3250965204243797760	12.7828	55.21712	-1.54672	-0.0158	0.6858	*Visual Binary
9	111607167	70286319462343808	11.74727	56.30801	26.5884	0.0390	0.5257	Variable(G)
10	480603181	65205166993246080	14.21742	56.58174	23.91762	-0.0482	0.5347	*Bright Star Pollution
11	100904105	65223618172733952	11.95708	56.6641	24.02969	0.0376	0.5394	*BY Dra Variable
12	204105048	163600634362268800	11.44613	60.13293	27.42786	0.0311	0.5155	*MS+WD Binary [1]
13	273916194	232362820257069440	10.37425	62.41018	43.59254	-0.0312	0.5814	Variable(K)
14	470205184	232914736434443136	14.58639	64.16136	45.60959	-0.0582	0.5370	
15	384509039	3285027799594151680	13.08165	65.08137	5.838964	0.0397	0.5265	Variable(K)
16	275203109	253742995657660288	10.77930	67.0192	45.56416	-0.0471	0.5171	Binary (G)
17	361716215	277067485569047680	11.67850	67.28308	55.21747	-0.0010	0.5058	Variable(K)
18	250801006	3405685422487373568	14.17399	73.94313	17.28189	0.0395	0.5380	Variable (G)
19	39104099	205354966385794048	12.32107	73.95885	43.69652	-0.0407	0.5201	Variable(K)
20	528007141	3228908790535918976	14.17989	75.26918	1.364525	0.0003	0.5315	Variable(G)
21	307304141	211681178338056192	12.04812	78.64506	45.42125	-0.0489	0.5924	Variable(K)
22	678513097	281149010170791552	14.78009	79.71296	59.046	0.0052	0.5139	Variable(G)
23	89713095	3448967285402131712	12.44196	82.39802	32.74561	0.0284	0.5200	*Nearby Star Pollution
24	208806168	3333163830247192064	12.34049	84.0461	6.520935	0.0056	0.5176	Variable(K)
25	393309119	3397615659976935296	11.66793	84.67204	18.00152	-0.0244	0.5161	
26	505215137	3216524342533541248	15.34401	85.14597	-2.19503	0.0140	0.7151	*Nebula Pollution
27	505204206	3216417655546088192	15.33606	85.17643	-2.84414	-0.0422	0.6781	*Nebula Pollution
28	297011180	189407787175600640	11.11371	85.21744	37.46183	-0.0046	0.5181	Variable(K)
29	505215105	3216425077249628544	14.59378	85.24724	-2.74513	-0.0240	0.5676	*Nebula Pollution
30	547505087	3399231147498442112	11.37671	85.84326	19.40144	-0.0061	0.5907	*Eclipsing Binary
31	127806031	3431388156057648128	11.96078	90.89316	28.81194	-0.0240	0.5169	*Chemically Peculiar Star/Nearby Star Pollution
32	486302167	3423621618233438080	14.50957	90.98312	21.90916	-0.0306	0.5206	
33	606202112	3375271831352365568	13.13685	91.74336	21.03054	0.0338	0.5124	Variable(K)
34	501916045	3328461188953301120	14.17653	91.90313	8.044743	0.0116	0.5105	
35	641111226	3345719467060096768	15.06539	92.92255	15.19583	0.0246	0.6064	
36	606211049	3426827038226866176	13.94504	93.65705	25.50473	-0.0098	0.5420	*RR Lyrae Variable
37	486809137	3425551463001195008	11.62234	94.2737	23.42387	0.0218	0.5791	Variable(K)
38	267811169	3370935975970328192	14.46051	95.64267	19.2116	-0.0069	0.5129	

[1] Ren et al. (2020)

39	696613240	3102733650797714816	12.25146	103.3226	-3.61788	-0.0450	0.5318	Giants with wrong logg (L)
40	378105061	993779054893891840	12.59996	104.1611	54.1417	0.0390	0.5606	Variable(K)
41	88605186	3109933798391183232	12.26119	110.448	-1.2325	0.0394	0.5217	Variable(K)
42	88805176	3109936826350414592	10.76796	110.5126	-1.13856	-0.0208	0.5129	*Spectral Binary
43	226703189	892715622559710592	14.19901	113.7437	33.00618	0.0167	0.5036	*MS+WD Binary [2]
44	93609075	3064639245085801344	12.01463	123.5568	-5.45447	-0.0004	0.5251	*Visual Binary/Variable(K)
45	308415140	3098139547613310720	12.97677	124.1939	8.390326	0.0338	0.5706	Variable(K)
46	656613008	636182586087691392	14.07274	136.9056	18.83429	-0.0199	0.5699	
47	201907064	3824325436834913920	11.80175	146.0101	-4.58495	0.0258	0.5085	Variable(G)
48	303015088	830588577026980992	11.67706	160.1215	46.73302	0.0117	0.5526	*High Proper Motion Star
49	401214096	3816910296057695232	12.01111	168.8487	5.573148	0.0217	0.5220	SB1 (L)
50	208509165	3695446967363569408	12.37765	188.6458	-1.01727	0.0078	0.5116	*Visual Binary
51	132212074	3650688086675908352	12.20117	221.798	-0.49315	0.0300	0.6415	*Hot Subdwarf
52	426805127	1597737184257054720	12.58121	233.8434	53.58372	0.0016	0.8177	Variable(K)
53	152601123	1353107529388288896	13.30084	252.5303	40.17427	-0.0424	1.1223	Cosmic Ray Pollution(L)
54	334701053	1360809745779585152	12.16614	262.6004	44.48631	0.0259	0.5065	Variable(K)
55	574714131	2133632795086109440	14.42111	286.6875	50.6358	-0.0180	0.5585	
56	243012154	2102151990479456128	12.88417	287.9217	41.05147	-0.0023	0.5427	*Nearby Star pollution
57	369703082	2099502579773618560	12.64614	289.1561	39.14371	0.0001	0.5057	*Visual Binary
58	52403133	2101074331648268032	13.70564	290.483	39.73531	-0.0138	0.5461	
59	580505166	2052645379929910144	13.74717	290.9112	38.33558	0.0236	0.5094	Variable(G)
60	362811058	2134979074057185408	13.58594	295.6626	50.14518	0.0383	0.5129	*Rotating Variable/Visual binary
61	355104179	2079247720169124992	14.78923	299.1187	45.4898	0.0077	0.6236	*Pulsating Variable
62	158908013	2082103770340838144	13.23867	300.7669	44.86653	-0.0210	0.5786	*Rotating Variable
63	260702136	2068072279678698112	13.12818	306.8594	41.61058	0.0105	0.5884	*Nearby Star Pollution? Variable(G)
64	587915134	2163026176885565568	14.99146	314.1843	44.80388	-0.0093	0.6707	*Nebula Pollution
65	169005207	1781458323057855360	12.24709	331.3152	20.28735	0.0262	0.6259	*Visual Binary
66	75308136	2735568299794226304	11.86591	335.6045	15.65098	-0.0004	0.5444	*Visual Binary
67	75308129	2735577375059931264	12.50423	335.722	15.78769	-0.0179	0.5357	
68	270405145	2008973392251158784	14.50971	345.2708	55.97517	-0.0224	0.5878	*Nearby Star Pollution
69	387904014	2664836171318493696	14.05540	349.4505	7.379211	0.0254	0.6097	*Hot Subdwarf Candidate / UV excess
70	180206182	1924190810839989632	12.92156	350.0968	40.73101	-0.0105	0.9052	*Visual Binary

NOTE—In the classification, asterisks ”*” indicate sources that have been identified through the visual examination of relevant information in CDS website, such as SIMBAD information, literatures, SEDs and images; ”Varaiable (G)” and ”Binary (G)” are targets cross matched with `gaiadr3 variability` (Rimoldini et al. 2023) and `gaiadr3 non-single stars` (Holl et al. 2023) databases respectively; ”Varable(K)” stands for stars show apparent variations in Kepler or Tess light curves by visual inspection, as some of them showing periodic variations, binaries could not be excluded. ”(L)” means the judgement is derived by inspecting the LAMOST spectra.

[2] Gentile Fusillo et al. (2015)